Supplementary Information: Superconducting cavity-based sensing of band gaps in 2D materials

Krishnendu Maji,[1] Joydip Sarkar,[1] Supriya Mandal,[1] Sriram H,[1] Mahesh Hingankar,[1] Ayshi Mukherjee,[1] Soumyajit Samal,[1] Anirban Bhattacharjee,[1] Meghan P. Patankar,[1] Kenji Watanabe,[2] Takashi Taniguchi,[3] and Mandar M. Deshmukh[1,*]

[1]*Department of Condensed Matter Physics and Materials Science, Tata Institute of Fundamental Research, Homi Bhabha Road, Mumbai 400005, India.*

[2]*Research Center for Functional Materials, National Institute for Materials Science, 1-1 Namiki, Tsukuba 305-0044, Japan.*

[3]*International Center for Materials Nanoarchitectonics, National Institute for Materials Science, 1-1 Namiki, Tsukuba 305-0044, Japan.*

CONTENTS

* deshmukh@tifr.res.in

1. DEVICE FABRICATION

1.1. Fabrication of the cavity

The device is fabricated on SiO_2 (280 nm)/intrinsic Si (500 μm) substrate. The substrate is initially DC magnetron sputtered with 50 nm MoRe, a type-II superconductor in a high-vacuum chamber ($\sim 3 \times 10^{-7}$ mbar) with a sputtering pressure of $\sim 2 \times 10^{-3}$ mbar. Then, photolithography and SF_6 (12.5 sccm)/Ar (10 sccm) reactive ion etching are used to pattern the $\lambda/2$ SCPW cavity onto the substrate. For the fabrication of the LP filters electron beam lithography is used instead of photolithography.

1.2. Fabrication of the BLG heterostructure

To make the hBN-BLG-hBN stack we exfoliate graphene and hBN flakes using scotch tape mechanical exfoliation technique. We choose suitable bilayer graphene flakes based on optical contrast. The hBN flakes of suitable thicknesses are selected based on color under an optical microscope and later thickness is confirmed by AFM after the device is completed. Subsequently, the flakes are assembled individually using poly(bisphenol A carbonate)/polydimethylsiloxane stamps. Then we drop the stack on the cavity. Next, we use standard electron-beam lithography followed by Aluminum deposition by evaporation at high vacuum ($\sim 2.5 \times 10^{-7}$) to make the top gate and electrode to bias the BLG.

2. MEASUREMENT DETAILS

Figure S1 show the circuit diagram of the measurement. The measurements are done in an Oxford dilution fridge at 20 mK. The input signal is attenuated by 60 dB using a series of attenuators kept at different plates of the dilution fridge for proper thermalization of the photons reaching the device. The output signal is amplified through a 40 dB high-electron-mobility-transistor (HEMT) amplifier kept at the 4 K plate, followed by a 23 dB room temperature amplifier (Mini-circuits). The measurements are done using a Rohde and Schwarz vector network analyzer (ZNB20). The DC voltage to the top gate is applied through a 10 Hz low-pass filter and combined with the output RF line using a bias tee. The DC voltage to the back gate is applied similarly which is not shown in the

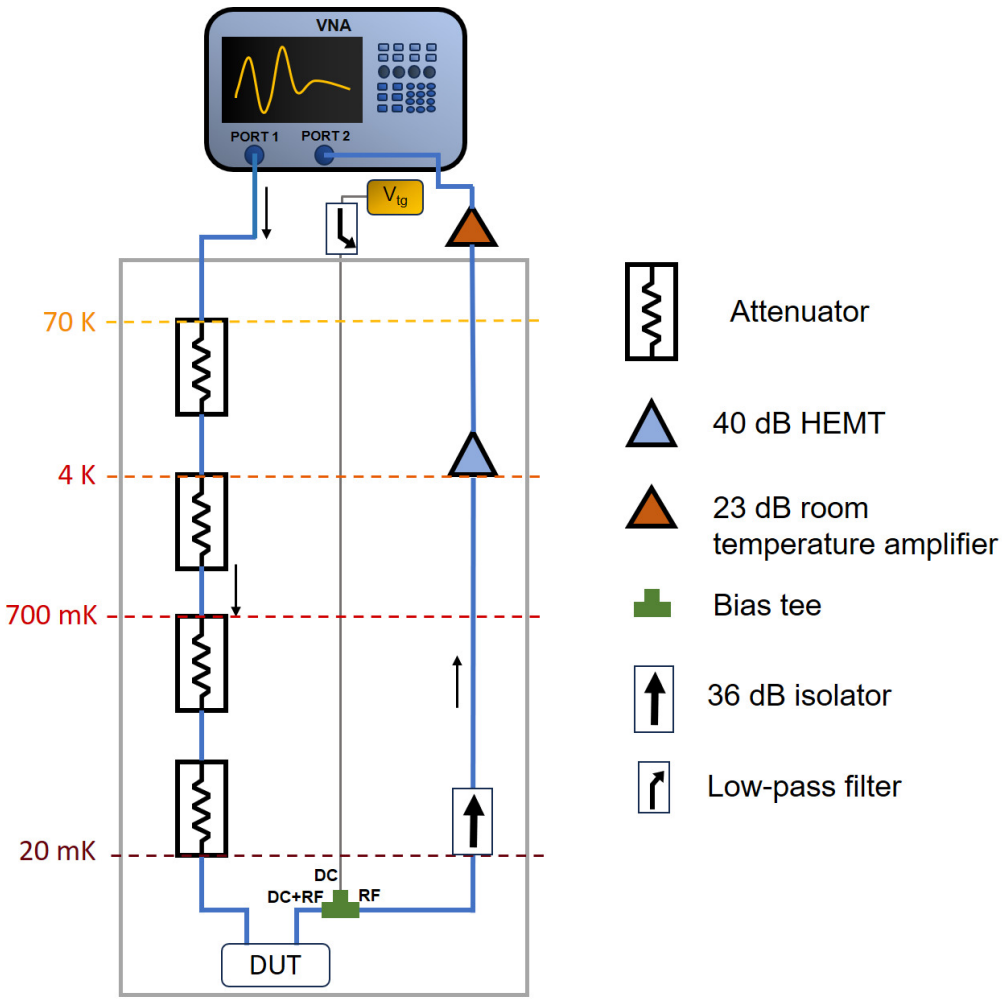

Supplementary Fig. S1: Microwave measurement setup. Shows the wiring diagram for the measurement. The input microwave signal is sent to the device from port 1 of the VNA through a series of attenuators kept at different plates of the dilution fridge. The output signal is amplified through a 40 dB high-electron-mobility-transistor (HEMT) amplifier followed by a 23 dB room temperature amplifier before reaching port 2 of the VNA. The DC voltage is applied to the top gate through a 10 Hz low-pass filter.

schematic.

3. COMSOL SIMULATION

The finite element simulation has been performed using COMSOL to find the cavity modes. In Figure S2 the amplitude of the simulated transmission coefficient, $|S_{21}|^2$ of the

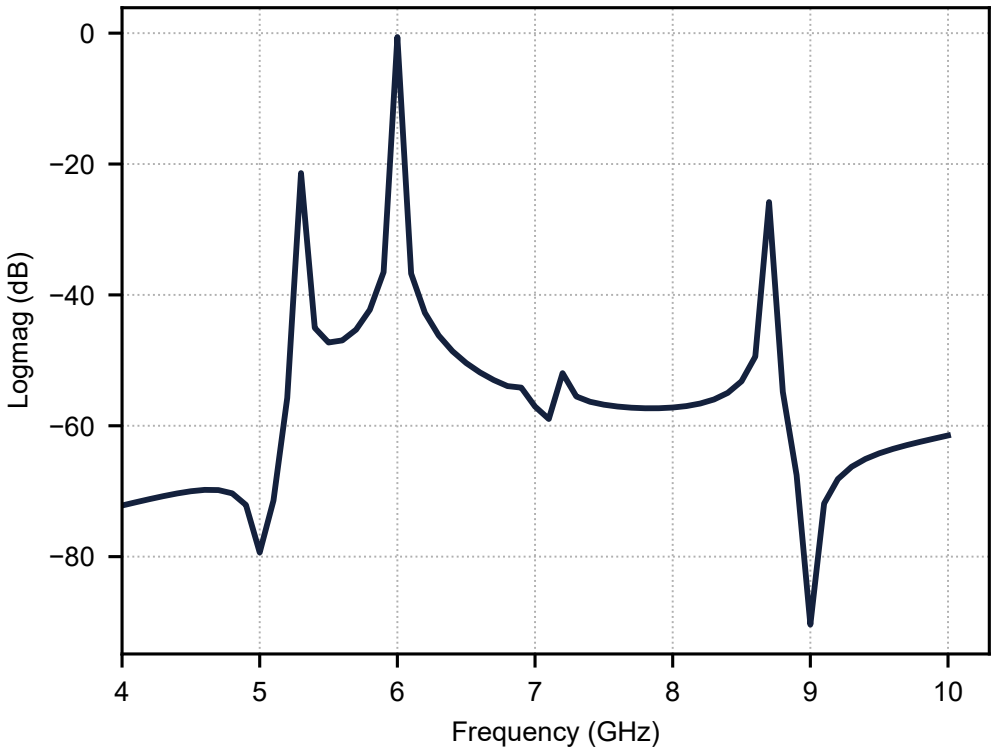

Supplementary Fig. S2: COMSOL simuation Simulated amplitude of the transmission coefficient ($|S_{21}|^2$) of the cavity. The simulation was done in COMSOL Multiphysics software.

.

cavity is shown. The transmission peak which touches 0 dB is the mode of our interest, and it matches well with the experimental data.

4. ADDITIONAL DATA

4.1. Data at a fixed frequency

For each (V_{TG}, V_{BG}), transmission is measured at a frequency of 5.151 GHz. In Figure S3 a the amplitude of the transmission coefficient, $|S_{21}|^2$ is plotted as a function of (V_{TG}, V_{BG}). Notably, there is a finite offset in both V_{BG} and V_{TG} axes due to charge doping from the metallic gates which have been discussed in detail in the main text. The data in Figure S3 a is transformed to (n, D/ϵ_0) plane in Figure S3 b. In Figure S3 c the phase of the transmission coefficient, $\angle S_{21}$ is plotted as a function of (V_{TG}, V_{BG}). The data in Figure S3

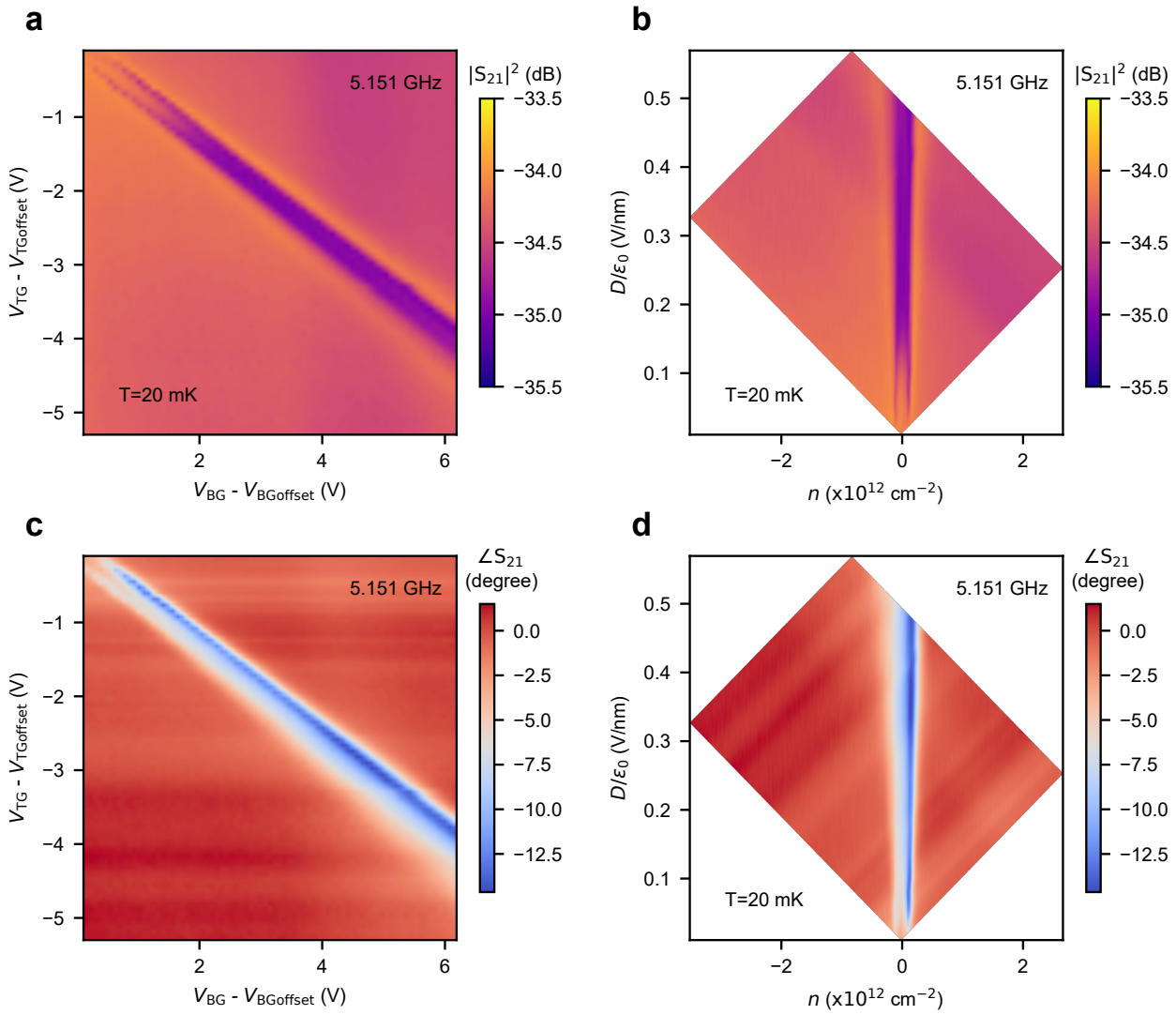

Supplementary Fig. S3: Additional data. a,The amplitude of the transmission coefficient, $|S_{21}|^2$ at frequency 5.151 GHz is plotted as function of (V_{TG}, V_{BG}). There is a finite offset in both V_{BG} and V_{TG} axes due to charge doping in BLG from the metallic gates. **b,** The data in panel **a** is shown in (n, D/ϵ_0) plane. **c,** The phase of the transmission coefficient, $\angle S_{21}$ at frequency 5.151 GHz is plotted as a function of (V_{TG}, V_{BG}). **d,** The data in panel **c** is shown in (n, D/ϵ_0) plane.

c is transformed to (n, D/ϵ_0) plane in Figure S3 d.

4.2. Data in the negative displacement field sector

The data was collected in the negative displacement field sector also. In Figure S4 a, we have plotted the full data in the (V_{BG}, V_{TG}) plane. The plot in Figure S3 a is transformed to

$(n,\ D/\epsilon_0)$ plane from $(V_{\mathrm{BG}},\ V_{\mathrm{TG}})$ plane in Figure S4 b. A peak in the transmission appears parallel to the V_{TG} axis. This feature appears from the part of the device where only the bottom gate does gating to the bilayer graphene. Also, there is some bending of the BLG gap opening feature in the negative displacement sector. We do not fully understand the reason for this bending.

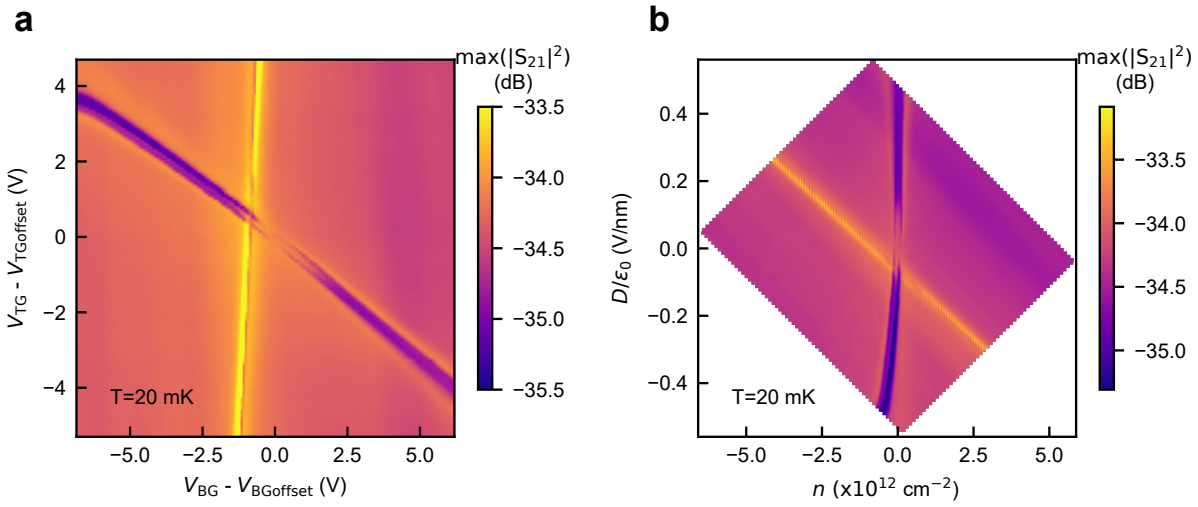

Supplementary Fig. S4: Data in both the positive and negative displacement field sectors. **a,** For each $(V_{\mathrm{TG}},\ V_{\mathrm{BG}})$ the transmitted signal through the cavity is measured as a function of frequency. The peak value of the amplitude of the transmission coefficient, $|\mathrm{S}_{21}|^2$ is plotted as a function of V_{TG} and V_{BG}. A finite offset in both V_{TG} and V_{BG} axes is due to charge doping in BLG from the metallic gates. **b,** $\max(|\mathrm{S}_{21}|^2)$ is plotted as a function of n and D/ϵ_0.

4.3. van-Hove singularity-like feature

For each $(n,\ D/\epsilon_0)$ point, the transmitted signal through the cavity is measured as a function of frequency. In Figure S5 a, the peak value of the amplitude of the transmission coefficient, $|\mathrm{S}_{21}|^2$ is plotted as a function of n and D/ϵ_0. The line slice of $|\mathrm{S}_{21}|^2$ with n for D/ϵ_0=0.2, 0.3, 0.4 V/nm is shown in Figure S5 b. For all of the D/ϵ_0, we can see a van-Hove singularity-like feature; a peak in the signal next to the gap regions appears. However, the van-Hove singularity-like features are not so prominent in the capacitance (C_2) and d_g plots (Figure 4 c and e respectively in the main manuscript). In future works, this could be

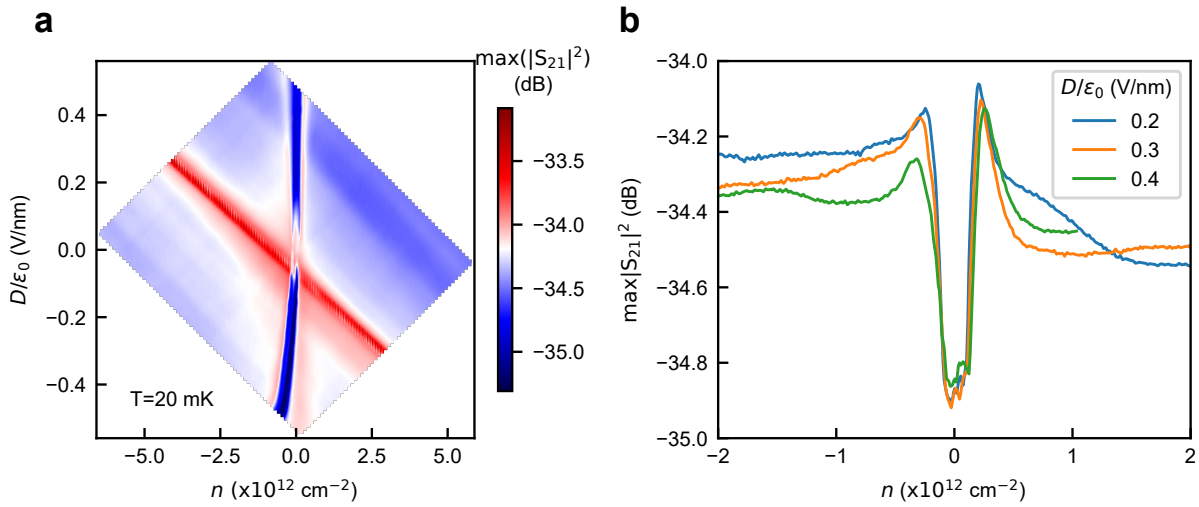

Supplementary Fig. S5: Possible signature of van-Hove singularities in BLG. a, For each (n, D/ϵ_0) the transmitted signal through the cavity is measured as a function of frequency. The peak value of the amplitude of the transmission coefficient,$|S_{21}|^2$ is plotted as a function of n and D/ϵ_0. **b,** Shows the line slice of $|S_{21}|^2$ with n for $D/\epsilon_0 = 0.2, 0.3, 0.4$ V/nm.

captured by improving the fitting model and fitting accuracy to extract the capacitance.

As the area of our device is relatively larger $\sim$30 μm^2, there is an inhomogeneous variation in charge density (n). This variation in n may smear out the van Hove singularities at the band edge to some extent[1]. The observed inhomogeneous variation in n has been reported in previous studies, contributing to the absence of van Hove singularities in the data [2].

5. FITTING PROCEDURE

First, the frequency line-slice for a particular ($V_{\rm BG}$, $V_{\rm TG}$) is fitted with Equation 1 in the main text keeping C_2, Q_i, skewness factor s, b, and ω_0 as the fitting parameters. From the fitting, we get ω_0=5.285 GHz. Then, for each combination of ($V_{\rm BG}$, $V_{\rm TG}$), the frequency line-slice data is subjected to fitting with C_2, Q_i, skewness factor s, and b as the fitting parameters keeping ω_0 constant. The ω_0 is kept constant so that the resonant frequency shifts only due to the capacitive loading of C_2, and is not influenced by the change in bare resonant frequency ω_0. Figure S6 a and b show the extracted capacitance C_2 and the error in C_2 from the fitting respectively. In Figure S6 b there are some white patches, at those

points, the error in C_2 from the fitting diverges.

To elucidate the impact of capacitive loading on the resonant frequency, we derive the expression for the resonant frequency from Equation 1 in the main text under certain assumptions. Substituting the expressions for A, B, C, and D into Equation 1 yields:

$$\mathrm{S}_{21} = \frac{4\omega^2 Z_0^2 C_1 C_2}{(2j\omega Z_0 C_1 + 1)(2j\omega Z_0 C_2 + 1)e^{\gamma l} - e^{-\gamma l}}. \tag{1}$$

Assuming the ω is very close to the bare resonant frequency ω_0, the Equation 1 is simplified to

$$\mathrm{S}_{21} \approx \frac{\frac{4\omega^2 Z_0^2 C_1 C_2}{\pi}}{\left(\frac{1}{Q_i} - \frac{4\omega^2 Z_0^2 C_1 C_2}{\pi} - \frac{2\omega Z_0 (C_1+C_2)\Delta}{\omega_0}\right) + j\left(\frac{2\omega Z_0 (C_1+C_2)}{\pi} + \frac{2\Delta}{\omega_0}\right)}. \tag{2}$$

The resonant frequency, ω_r can be obtained by setting $\mathrm{Im}(\mathrm{S}_{21}) = 0$, which gives

$$\omega_r = \omega_0 - \frac{\omega_0 \omega_r Z_0 (C_1 + C_2)}{\pi}. \tag{3}$$

We can calculate ω_r by solving Equation 3 iteratively. From Equation 3 it is evident that the resonant frequency ω_r decreases with an increase in C_2.

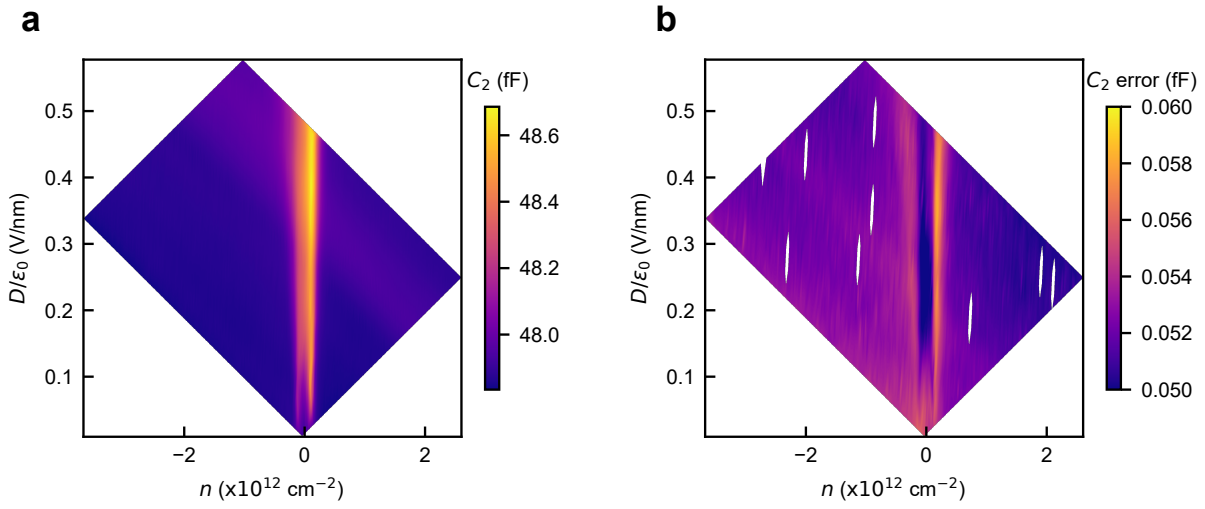

Supplementary Fig. S6: Error in the extraction of the capacitance from the fitting. a, Shows the extracted capacitance C_2 from the fitting as a function of n and D/ϵ_0. **b,** Shows the error in C_2 from the fitting.

6. ATOMIC FORCE MICROSCOPY OF THE HBN FLAKES

Atomic force microscopy(AFM) of the top and bottom hBN flakes has been performed, which are shown in Figure S7 a and b respectively. Panels c and d show the line slices along the white line in panels a and b respectively. The thicknesses of the top hBN and bottom hBNs are 32.9 ± 0.6 nm and 50.1 ± 1 nm respectively. respectively.

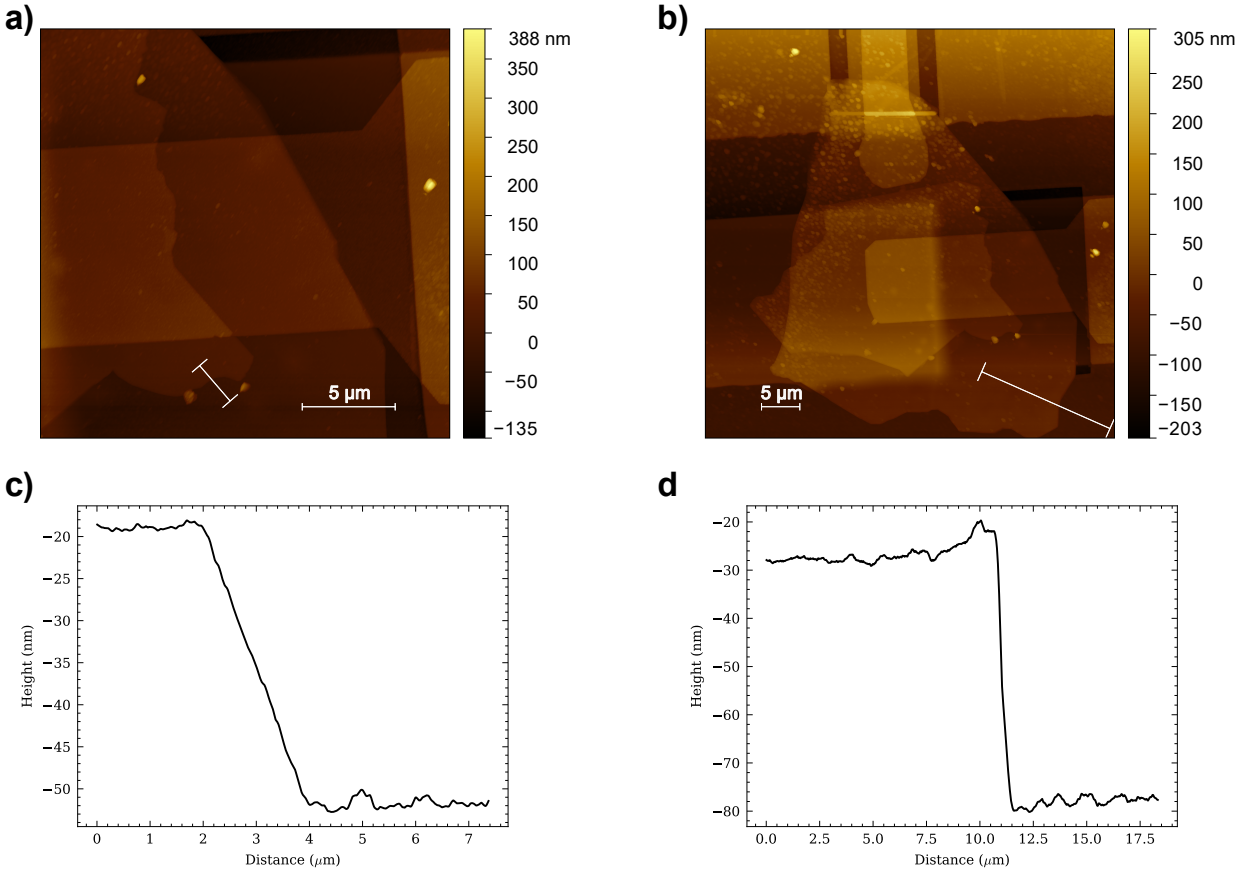

Supplementary Fig. S7: AFM data of top and bottom hBNs. **a** and **b** show the AFM data of the device from which the thickness of the top and bottom hBNs has been extracted respectively. **c** and **d** are the line slices along the white line in panel **a** and **b** respectively.

7. COMPARISON WITH OTHER WORKS

In Table I, we have compared our technique with other state-of-the-art techniques to measure the capacitances of 2D heterostructures.

Paper	**How the capacitance is measured/extracted**	**Accuracy**	**Frequency range**
Electronic compressibility of layer-polarized bilayer graphene, A. F. Young et. al.[1]	They measured the top gate capacitance (capacitance between the top gate and the graphene) by applying a small AC signal to the top gate and measuring the current through the graphene.	The capacitance measurement has a resolution of sub femtofarad.	Not mentioned
Measurement of the electronic compressibility of bilayer graphene, E. A. Henriksen et. al.[2]	They measured the penetration field capacitance i.e., they measured the capacitance of the back gate to the top gate, where the electric field lines between the gates penetrate the grounded graphene sheet. They measured it by applying a small AC signal to the back gate and recording the resulting current through the top gate.	They fitted their capacitance data using Equation 2 in our main manuscript. They calculated d_g from a tight-binding model and varied the stray capacitance until the best fit was obtained.	300-1000 Hz

Direct measurement of discrete valley and orbital quantum numbers in bilayer graphene, B.M Hunt et. al.[3]	They measured both the top gate capacitance (C_T) and bottom gate capacitance (C_B), from which they calculated their symmetric (C_S) and anti-symmetric (C_A) combination as C_S C_T + C_B, and C_A C_T - C_B. To measure $C_{B(A)}$, two synchronized and nearly equal-magnitude AC signals (δV_{EX}) are applied to the top and bottom gates.	They have not explicitly mentioned the accuracy or sensitivity of their capacitance measurement. They used a standard capacitor C_{std} = 404 fF. The measured C_S varies between 141.4 fF and 260.2 fF and C_A varies between -1.6 fF and 1.6 fF.	67.778 kHz
Spin–orbit-driven band inversion in bilayer graphene by the van der Waals proximity effect, J. O. Island et. al.[4]	They measured C_P between the top and bottom gates of their BLG-WSe_2 heterostructure using a low-temperature capacitance bridge. C_P is measured by applying a fixed AC excitation to the top gate (δV_{TOP}). The phase and amplitude of a second AC excitation with the same frequency are adjusted and applied to a standard reference capacitor (C_{ref}) on the low-temperature amplifier to balance the capacitance bridge.	They have plotted the C_P in arbitrary units but have not mentioned the accuracy in their capacitance measurement.	17-33 kHz

Half- and quarter-metals in rhombohedral trilayer graphene, H. Zhou et. al.[5]	They measured the penetration field capacitance C_P between the top and bottom gates of their device using a low-temperature capacitance bridge by applying a small AC excitation to the top gate.	Measurement accuracy is not mentioned.	10-55 kHz
Isospin magnetism and spin-polarized superconductivity in Bernal bilayer graphene, H. Zhou et. al.[6]	They measured the penetration field capacitance C_P of their bilayer graphene device using a low-temperature capacitance bridge by applying a small AC excitation to the top gate.	Measurement accuracy is not mentioned.	54.245 KHz
This work	We measured the penetration field capacitance C_P of the BLG heterostructure coupled with a superconducting coplanar waveguide cavity. By fitting the transmission data through the cavity using the ABCD transmission matrix model, we extract the value of the capacitance of the heterostructure.	The measured capacitance varies between 47.8 fF to 48.7 fF. The error in the capacitance from the fitting varies between 0.05 fF to 0.06 fF.	1-10 GHz

TABLE I: Comparison table

8. DENSITY OF STATES CALCULATION OF BILAYER GRAPHENE

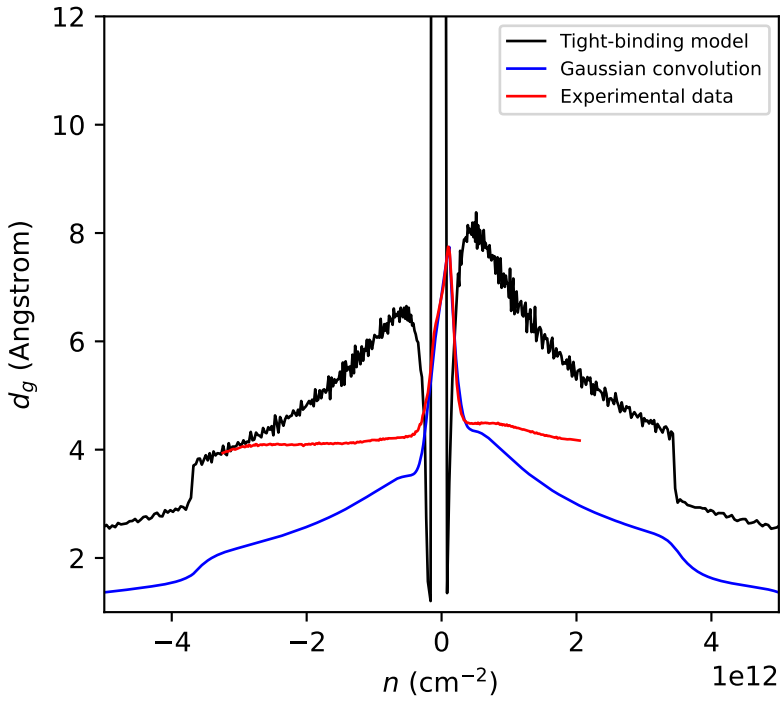

Supplementary Fig. S8: Comaparison with theory. The black curve is the calculated d_g of BLG from the tight-binding model. The $d_g = \frac{\epsilon_0}{e^2}\frac{\partial \mu}{\partial n}$ is obtained from the tight-binding model of BLG[7] in presence of a perpendicular displacement field D/ϵ_0=0.3 V/nm and inter-layer coupling γ_4=0.14 eV. The blue curve is the convolution of d_g with a Gaussian function with variance $\delta n = 1.6 \times 10^{11}$ cm^{-2}. The red curve is the experimentally derived d_g at D/ϵ_0=0.3 V/nm.

To compare our data with theory, we calculated the density of states ($\frac{\partial n}{\partial \mu}$) of BLG from the tight-binding model[7], from which we derived d_g with the formula $d_g = \frac{\epsilon_0}{e^2}\frac{\partial \mu}{\partial n}$. In Figure S8, the black curve shows the calculated d_g from the tight-binding model in the presence of a displacement field D/ϵ_0=0.3 V/nm, and inter-layer coupling γ_4 =0.14 eV. Since our device area is relatively larger ∼30 μm^2, there is a variation of n across the device. To incorporate this, we have convolved the calculated d_g with a Gaussian with variance, $\delta n = 1.6 \times 10^{11}$cm^{-2}, which is shown in the blue curve. The Gaussian convolution smoothens the van-Hove singularity features appearing on the band edge of BLG. This matches qualitatively well with the experimental data (shown in the red curve) at low

densities, but at higher densities, the matching is increasingly poor, as reported in previous studies[2].

[1] A. F. Young, C. R. Dean, I. Meric, S. Sorgenfrei, H. Ren, K. Watanabe, T. Taniguchi, J. Hone, K. L. Shepard, and P. Kim, Electronic compressibility of layer-polarized bilayer graphene, Physical Review B **85**, 235458 (2012).

[2] E. A. Henriksen and J. P. Eisenstein, Measurement of the electronic compressibility of bilayer graphene, Physical Review B **82**, 041412 (2010).

[3] B. M. Hunt, J. I. A. Li, A. A. Zibrov, L. Wang, T. Taniguchi, K. Watanabe, J. Hone, C. R. Dean, M. Zaletel, R. C. Ashoori, and A. F. Young, Direct measurement of discrete valley and orbital quantum numbers in bilayer graphene, Nature Communications **8**, 948 (2017), number: 1 Publisher: Nature Publishing Group.

[4] J. O. Island, X. Cui, C. Lewandowski, J. Y. Khoo, E. M. Spanton, H. Zhou, D. Rhodes, J. C. Hone, T. Taniguchi, K. Watanabe, L. S. Levitov, M. P. Zaletel, and A. F. Young, Spin–orbit-driven band inversion in bilayer graphene by the van der Waals proximity effect, Nature **571**, 85 (2019), number: 7763 Publisher: Nature Publishing Group.

[5] H. Zhou, T. Xie, A. Ghazaryan, T. Holder, J. R. Ehrets, E. M. Spanton, T. Taniguchi, K. Watanabe, E. Berg, M. Serbyn, and A. F. Young, enHalf- and quarter-metals in rhombohedral trilayer graphene, Nature **598**, 429 (2021), number: 7881 Publisher: Nature Publishing Group.

[6] H. Zhou, L. Holleis, Y. Saito, L. Cohen, W. Huynh, C. L. Patterson, F. Yang, T. Taniguchi, K. Watanabe, and A. F. Young, Isospin magnetism and spin-polarized superconductivity in Bernal bilayer graphene, Science **375**, 774 (2022), publisher: American Association for the Advancement of Science.

[7] E. McCann and M. Koshino, The electronic properties of bilayer graphene, Reports on Progress in Physics **76**, 056503 (2013), publisher: IOP Publishing.

bibliography